




TECHNICAL ARTICLE

Experimental and Computational Thermal Analysis of Ti-Based Alloy Produced by Laser Metal Deposition Technique

L. RUDOLF KANYANE ^{1,4} NICHOLUS MALATJI,¹
A. PATRICIA POPOOLA,¹ S. ABIOLA RAJI,¹ SISA PITYANA,²
M. BRENDON SHONGWE,¹ and MONNAMME TLOTLENG^{2,3}

1.—Department of Chemical, Metallurgical and Materials Engineering, Tshwane University of Technology, P.M.B. X680, Pretoria, South Africa. 2.—Laser Materials Processing Group, National Laser Center CSIR, Pretoria 0001, South Africa. 3.—Materials Science Innovation and Modelling Research Group, North-West University, Mahikeng 2745, Mmabatho, South Africa. 4.—e-mail: LRkanyane@gmail.com

A Ti-Fe-Si-Cr-Nb alloy was fabricated using laser metal deposition (LMD) technique. The laser power and scanning speed were varied during fabrication to optimize the processing parameters. The thermal behavior during LMD processing was modeled and simulated by means of COMSOL Multiphysics 6.0 software. The samples produced were characterized using an optical microscope, X-ray diffractometer, and scanning electron microscope coupled with energy dispersive spectroscopy. The microhardness and wear behavior of the alloy were tested using a diamond indenter and ball-on-disk wear machine. The results obtained showed that the alloys exhibited similar dendritic microstructure for all processing parameters. The formation of cracks and pores were evident mainly in samples that were produced at high scanning speed and low laser power. A decrease in microhardness was noticed when the laser power was increased, while an increase in scanning speed yielded samples with high microhardness values. The alloy showed good tribological behavior, but no clear relationship between the wear resistance of the alloy and the variation of the laser processing parameters could be established.

INTRODUCTION

The excellent properties that are exhibited by titanium (Ti) and its alloys make them applicable for a variety of applications in the aerospace industry. This is due to their high specific strength-to-weight ratio, good corrosion resistance, high thermal stability, and oxidation resistance.¹⁻⁴ However, these alloys are characterized by low hardness and poor tribological properties which limit their adoption in demanding structural applications.^{5,6} For this reason, researchers have incorporated various alloying elements into the Ti matrix to improve the alloys' properties. These alloying elements either stabilize the formation of a single solid-solution structure or induce precipitation of a

secondary phase. Alloying elements such as aluminum (Al), vanadium (V), iron (Fe), manganese (Mn), molybdenum (Mo), niobium (Nb), and chromium (Cr) have been reported to act as stabilizers for both the β - and α -phases in Ti alloys. When these alloying elements are added to the Ti matrix, they either act as substitutional or interstitial solutes in the crystal lattice. Their presence in the matrix induces distortion of the crystal lattice, leading to a reduction in the movement of dislocations which brings about an improvement in the mechanical properties of the alloys.⁷⁻¹²

The incorporation of Nb in the Ti matrix was reported to stabilize the formation of the β -phase (bcc) with high strength but low ductility.¹³ On the other hand, the addition of Fe, tin (Sn), and Nb in the Ti matrix yielded positive synergetic effects on the microstructure and mechanical properties of the alloys, and the alloys obtained exhibited a single β -phase structure with superior mechanical strength

(Received May 29, 2023; accepted February 2, 2024;
published online February 20, 2024)

and ductility. The alloying elements were kept low enough not to trigger precipitation of intermetallic phases.¹⁴ Wang and Dong,¹⁵ successfully fabricated a Ti-Fe-Zr alloy which had a fine dendritic microstructure with average microhardness values of about 1000 HV for a zirconium (Zr) content of about 7.1 at.%, exhibiting β -phases for all the samples containing Zr.

Some alloying elements, such as silicon (Si), carbon (C), and nitrogen (N), do not form solid-solution structures when they are added to the Ti matrix due to the large differences in their atomic radii, which reduces their ability to form solid solutions and favors the formation of intermetallics. These intermetallic phases, such as titanium silicide (Ti_5Si_3), possess high hardness and good wear properties.^{16–19} The incorporation of Si in a Ti-Al alloy refined the microstructure and increased the microhardness. Alloys with a high Al:Si ratio have a high proportion of dispersive phases while the microhardness values could reach up to 900 HV for the alloys compared to 600 HV of the pure Ti-Al alloy. The increase in the microhardness of the alloys was attributed to the presence of the Ti_5Si_3 intermetallic compound.²⁰

Another way to manipulate the properties of Ti alloys is by using fabrication techniques that favor the restriction of grain growth during processing. Among the different methods used to produce Ti alloys, laser additive manufacturing (LAM) produces small-grained microstructures that are characterized by improved mechanical properties. Several AM routes, such as selective laser melting, electron beam melting, and laser metal deposition (LMD) have been successfully adopted to fabricate different metals and alloys like steels, Ni-based superalloys, titanium alloys, metal matrix composites, and bimetallic materials.^{21–30} However, LMD has the advantage of reduced material waste and other post-processing which makes it amenable to produce 3D parts and to repair worn components, hence, there is high interest in the adoption of this technique. The LMD process is associated with high solidification rates which result in the formation of fine microstructural grains. However, they also generate residual stresses and microstructural anomalies. Therefore, producing materials with defect-free microstructures and good mechanical properties requires the identification of optimized processing parameters for this type of AM route to be adopted.

Majumdar et al.²¹ successfully used a laser cladding process for the fabrication of titanium silicide dispersed in a titanium aluminide composite on a Ti-6Al-4V alloy substrate. The microhardness of the alloy was found to be dependent on the laser scanning speed. Slower scan speeds were associated with low microhardness properties, while higher microhardness values are usually recorded for fast deposition scan speeds. The build thickness, microstructure, and microhardness of the

Ti45Al5Nb0.5Si composite were found to be dependent on laser power, scanning speed, powder feed rate, and Si content. The thickness of the built samples increased with an increase in laser power and powder feed rate, but decreased with an increase in scanning speed. The low Si content in the alloy resulted in a defect-free microstructure for all laser powers. When the amount of Si was increased, microcracks were seen in the alloys produced at lower laser powers but they decreased with an increase in laser power. Low scanning speeds also yielded defect-free microstructures, and crack propagation was noticed with an increase in Si content and scanning speed. The hardness properties of the alloys were improved with an increase in scanning speed. The solidification rate of alloys during laser cladding is governed by the energy density of the deposited alloy samples:

$$E = \frac{P}{VHD} \quad (1)$$

where E is the energy density, P is the laser power, V is the scanning speed, H is the hatch spacing between two adjacent layers, and D is the diameter of the laser spot size.

The energy density of the deposited alloy samples increases with a decrease in scanning speed. High energy densities enable the high rate of melting of powder particles in the melt pool and allow diffusion of elements to occur.²² In the current study, a Ti alloy (Ti-Fe-Si-Cr-Nb) was developed using LMD. The aim of this work is to optimize the processing parameters and to analyze the developed alloy deposited on a Ti6Al4V substrate fabricated by the LMD process. Laser power and scanning speeds were optimized to produce the Ti-based alloy with a fine-grained microstructure and high mechanical properties. The effect of scanning speed and laser power on the microstructural evolution, phase formation, and tribological properties were investigated. The computational modeling of the Ti-based alloy's thermal behavior during the LMD process was simulated by means of COMSOL Multiphysics 6.0 software.

EXPERIMENTAL

Commercially pure elemental powders of Ti, Fe, Si, Cr, and Nb with a size range of 45–90 μm were mixed in a tubular mixer for 12 h and used as the precursor powder to produce the Ti9Fe5Si5Cr4Nb alloy by the LMD process. The samples were deposited on Ti6Al4V alloy plates of 100 mm \times 100 mm \times 10 mm using a Rofin-Sinar KUKA robot machine with 5-kW power. It uses a CO_2 laser to deposit the beam (beam diameter 1.5 mm) on the metal substrate, and the laser processing parameters are shown in Table I. Before deposition, the Ti6Al4V plates were sandblasted and cleaned with acetone to remove any debris on the substrates. The LMD technique deposits the metal powders via a

coaxial nozzle at a set speed and laser power, with argon as the shielding gas to protect the melt pool from contamination and oxidation. The deposition head moves along a tool path based on a predefined computer-aided design file. For more comprehensive understanding of the LMD process, the reader is referred to Refs. 13 and 23.

The microstructural and phase characteristics of the coatings were examined using a scanning electron microscope (SEM) equipped with energy dispersive spectroscopy (EDS) and an x-ray diffractometer (XRD). The microhardness of the samples was measured using a diamond indenter with a dwell time of 10 s and a load of 500 gf. A ball-on-disk wear tester was used to evaluate the friction and wear behavior of the samples. A load of 150 N and a sliding distance of 3 mm were used during the tests. The wear scars of the samples were studied using the SEM.

COMSOL Multiphysics 6.0 software was utilized to simulate the thermal behavior of the Ti-Fe-Si-Cr-Nb alloy during the LMD process. The software was used to create a model using the heat transfer in solids module incorporating temperature distribution during the layer build-up of 3 layers. Table II presents the model parameters used to model the thermal behavior during the LMD process. The rule of mixture was used to obtain the thermal properties of the alloy.²³ In the application of the rule, the Eq. 2 was applied:

$$M_{\text{alloy}} = \omega_{e1}M_{e1} + \omega_{e2}M_{e2} + \omega_{e3}M_{e3} + \omega_{e4}M_{e4} + s \quad (2)$$

where M_e is the material properties of each element incorporated in the alloy, ω_e is weight fractions of the elements, and M_{alloy} is the corresponding material property of alloy Ti9Fe5Si5Cr4Nb.

Governing Equations

The computational model reflects on heat transfer equations in the solid state for a 3-layered single track that simulates the LMD process in transient conditions. The model only considers temperature fields throughout the LAM of the Ti-based alloy by solving their governing equations under defined boundary conditions. Based on the heat transfer principle, the heat source of the LMD process presented is expressed by the Fourier heat differential by:

$$\rho C_p \frac{dT}{dt} + \rho C_p u \cdot \nabla T + \nabla \cdot q = Q \quad (3)$$

$$q = -k \nabla T \quad (4)$$

where ρ is the density of the alloy in kg/m^3 , C_p is the specific heat capacity at constant pressure in $\text{J}/(\text{kg K})$, T is the temperature (K), Q is the heat source intensity (J/mm^2), t is the time (s), u is the velocity field defined by the translational motion (m/s), q is the heat flux vector (W/m), and k is the coefficient of thermal conductivity ($\text{W}/(\text{m K})$); C_p and k change with temperature.

Gaussian distribution was used to present the heat source in the computational model.²⁴ To simplify the model and to closely represent the LMD manufacturing conditions, the following assumptions were made: (1) fluid flow dynamics are neglected, (2) no heat loss by conduction, (3) no material vaporization, and (4) the material is isotropic. A physics-controlled moving mesh with hyper-elastic smoothing was used. The mesh was a free tetrahedron mesh-type adopted for the laser scanning regions to achieve accurate results, while, in other regions, normal mesh size was used for proximity results.

Table I. Laser processing parameters and samples codes

Sample name	Power (W)	Scanning speed (m/min)
A	750	0.4
B		0.8
C		1.2
D	950	0.4
E		0.8
F		1.2
G	1150	0.4
H		0.8
I		1.2

Table II. Laser experimental properties and thermal properties of the Ti-based Alloy input in the model

Sample name	Power (W)	Scanning speed (m/min)	Laser spot size (mm)	Thermal conductivity (W/m)	Density (kg/m^3)	Specific heat capacity $\text{J}/(\text{kg K})$
C	750	1.2	3.0	21.6	4670	508.91
F	950					
I	1150					

RESULTS AND DISCUSSION

Phase Formation and Microstructural Evolution

Figure 1 presents the XRD patterns of the phases formed in the alloy, while Fig. 2 shows the optical microscope micrographs of the Ti-Si-Fe-Nb-Cr alloy fabricated at different laser processing parameters. The alloy exhibited α - and β -phases along with Ti_5Si_3 intermetallic phases formed during manufacturing via the reaction between the Ti and Si elements. The α -phase has the highest volume fraction of the phases present with a body-centered cubic (bcc) structure including the β -phase, while the Ti_5Si_3 as a hexagonal structure. These phases are known to promote potential high-temperature applications. The peak diffractions mostly follow the same pattern, with slight variations in intensities, which shows that the texture of the processed samples differs owing to the processing parameters used. Based on the work of Raji et al.,¹⁸ it can be deduced from the XRD results that the twinning occurs at 2θ between 45° and 70° due to the variation in energy densities. This was observed as the laser processing parameters changed, leading to broadening of the XRD peaks and reduction of the peaks' intensities, which is more visible especially in samples f and g. Thus, it was noted that the Ti-Fe-Si-Cr-Nb alloy displayed twinning effects, confirming that laser processing parameters affect planar faults. This is in conformity with other related literature.

Low laser scanning speeds produce alloys with high thickness and minimal surface defects. Cracks

are observed on samples fabricated at 750 W (Fig. 2a), but, as the laser power is increased to 950 W (Fig. 2d) and 1150 W (Fig. 2g), minimal defects were observed in the microstructure obtained. These samples show fewer pores compared to those that have been clad at scanning speeds of 0.8 m/min and 1.2 m/min for all powers. At low laser scanning speeds, heat input is increased and results in a simultaneous increase in energy densities. High energy densities create a large melt pool that allows more powder particles to be melted, resulting in alloy builds with increased thickness. Also, high temperatures are generated due to these conditions, thus reducing the cooling rate of the alloy during solidification. In these conditions, gases are allowed enough time to diffuse and to exit the alloy, leaving micropores on the surface. The high solidification rates associated with high scanning speeds are responsible for the formation of cracks, since the generation of residual stresses cannot be avoided with such conditions. Samples b, c, e, f, and h show the presence of some cavities. Due to rapid cooling at these scanning speeds, gases do not have enough time to escape and are trapped between the growing dendrites, leaving cavities in the microstructure. The cavities are predominantly near the heat-affected zone (HAZ) showing that the diffusion of gases is controlled by the direction of heat flow. The substrate acts as a heat sink during cladding, and the temperature drop occurs from the surface of the alloy towards the HAZ. Therefore, the trapping of gases will also be formed along this direction.

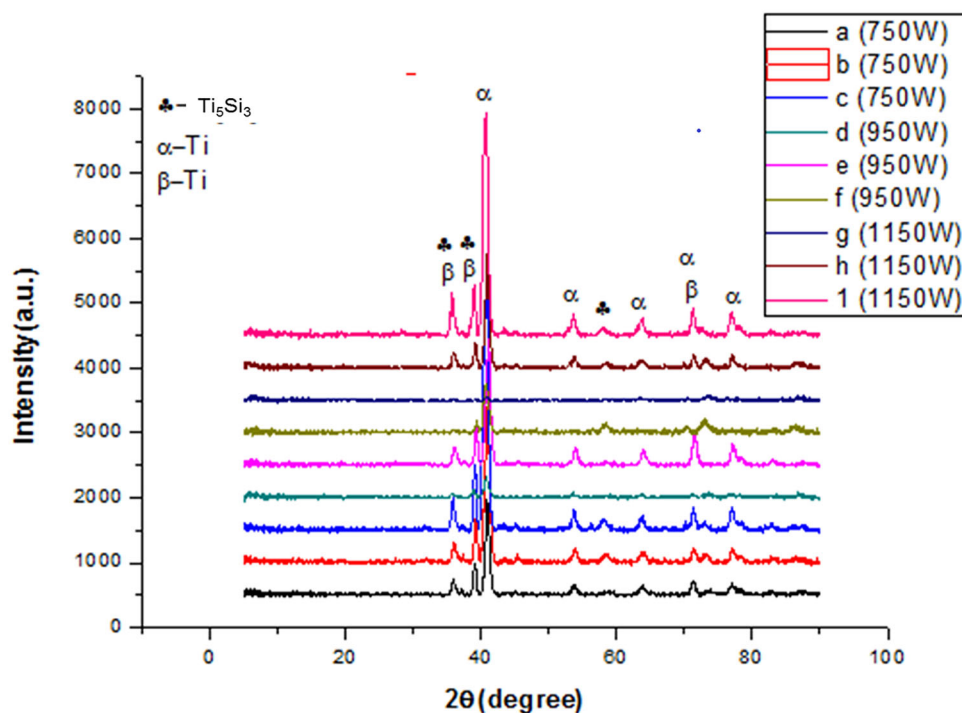


Fig. 1. XRD test result of coatings clad with different laser powers and scan speeds.

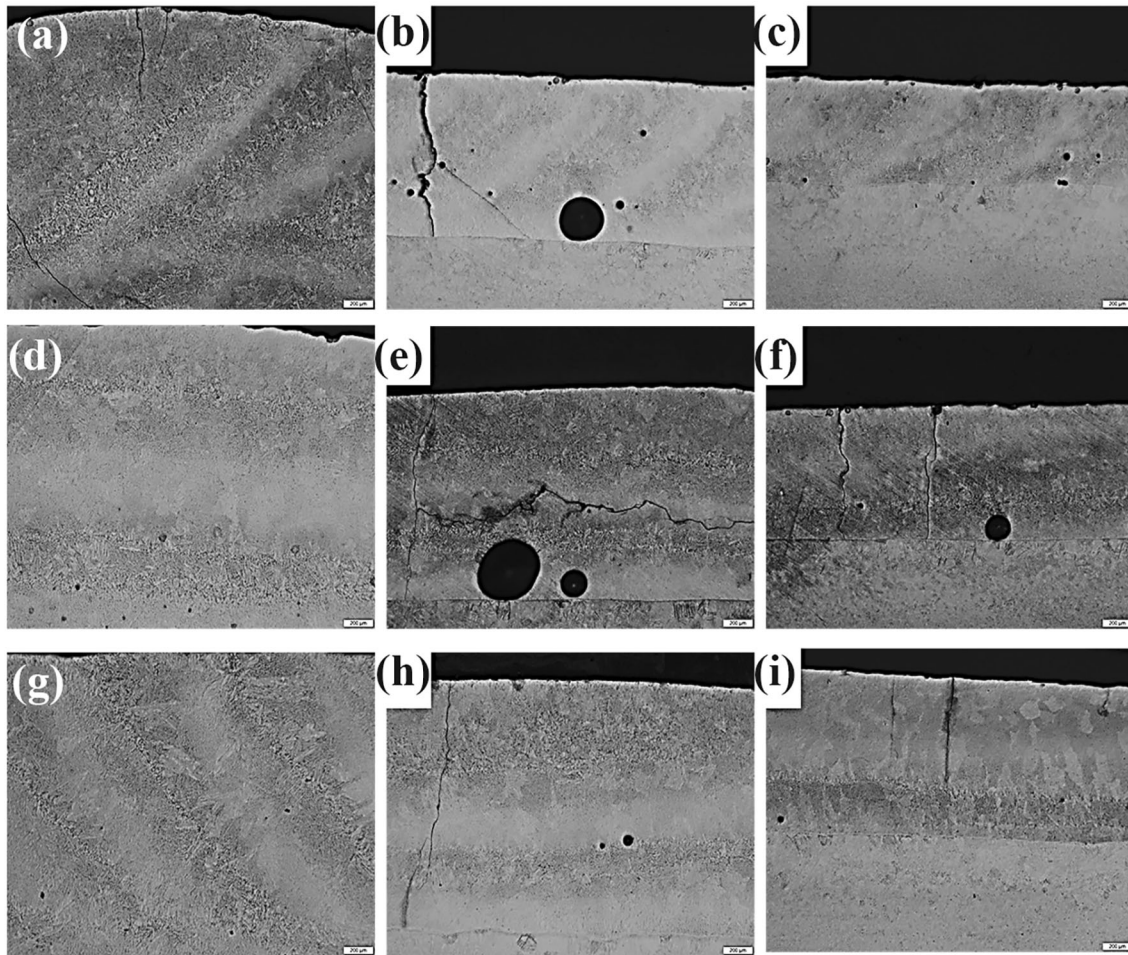


Fig. 2. Optical microscope micrographs obtained at the scanning speed of 0.4–1.2 m/min and laser power of: (a–c) 750 W; (d–f) 950 W; and (g–i) 1150 W.

The SEM images in Fig. 3 reveal the surface morphology of the alloys. All the samples exhibit microstructures with two distinct contrast regions (dendritic and interdendritic). It is evident that the laser processing parameters influence the refinement of the microstructures. Increasing the scan speed from 0.4–0.8 m/min to 1.2 m/min showed that grain refinement occurred at all laser powers. However, the increment of laser power from 750 W to 1150 W resulted in microstructures with coarser grains at all laser scan speeds. The coarsening and refinement of grains due to variations in laser power and scan speed occur as a result of the changing energy density. Nucleations of new atomic grains are lower when the energy density is high, creating a conducive environment for the growth of crystals, leading to the evolution of coarse microstructures. The strengthening mechanisms of the fabricated alloys is mainly dispersion strengthening caused by the β and Ti_5Si_3 reinforcements and solid-solution strengthening in the α -Ti matrix. This dispersion strengthening provided the most significant strengthening influence in this alloy. However, lower energy densities induce a high

solidification rate that results in rapid nucleation and the formation of microstructures with refined grains. Samples fabricated at higher laser scanning speeds and power reveal the presence of unmelted Nb particles. Nb is characterized by a high melting point of about 2400 °C and will require a very high energy density to be melted. The presence of cavities and pores is also observed and confirms the optical microscopy results. These defects are found to be dependent on the laser processing parameters. Samples produced at higher scanning speeds showed more pores and cavities than those fabricated at lower scanning speeds.

Thermal Behavior of Ti-Fe-Si-Cr-Nb Alloy During Laser Metal Deposition

Figure 4 present the laser thermal distribution of the Ti-Fe-Si-Cr-Nb alloy at 1.2 m/min and different laser powers (750 W, 950 W, and 1150 W, respectively). The heat build-up is as a result of the continual energy input which plays an important role in melt pool dimensions, cooling rate, and microstructural evolution. Consequently, it has a decisive influence on the mechanical performance of

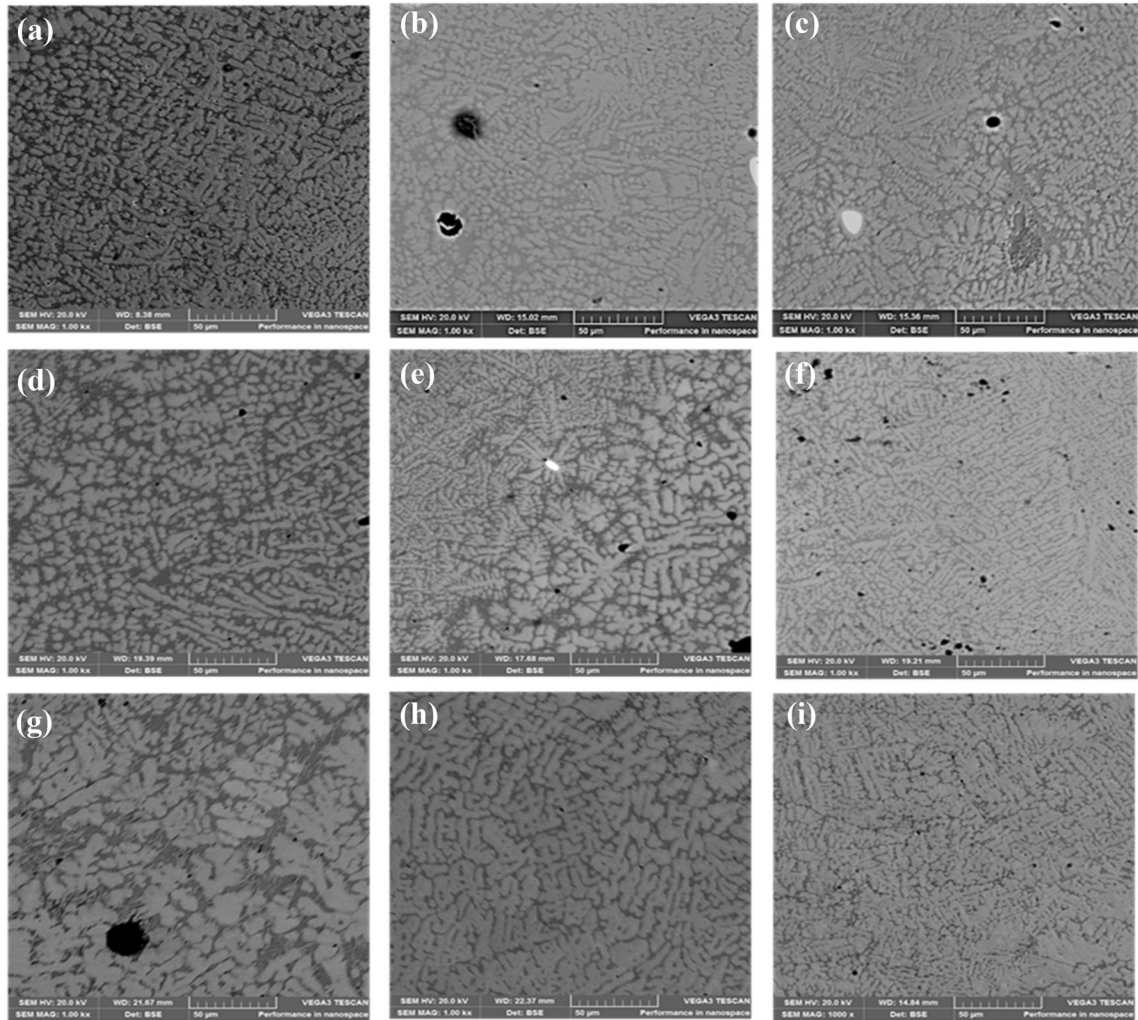


Fig. 3. Scanning electron microscope images of the Ti-Si-Fe-Nb-Cr alloy obtained at the scanning speed of 0.4–1.2 m/min and laser power of: (a–c) 750 W; (d–f) 950 W; and (g–i) 1150 W.

the synthesized alloys. It is clear that at 750-W laser power, the alloy’s overall surface temperature after 18 s was 1230 K, while at a high laser power, it reaches a maximum temperature of 1760 K. According to the literature, a combination of high laser scan speed and laser power leads to refined microstructures that are known for high microhardness properties owing to their high energy densities and fast cooling, thereby producing fine-grained microstructures.²⁵ The dynamics of the thermal process that occurs due to the effects of laser power on the Ti-Fe-Si-Cr-Nb alloy reveals that, during the LMD process, the morphological evolution of the alloys is dependent on the thermal history of the alloy samples. From the morphological evolution results compared to the computational thermal simulation results, it was noted that fine dendritic grains were achieved at 950 W (1.2 m/min), 1150 W (1.2 m/min), and 750 W (1.2 m/min). The initiation of stress and crack propagation can be observed in the 950-W (1.2 m/min) alloy (Fig. 2f). The high melting point associated with Nb and Cr is

responsible for decreasing the thermal gradients during fabrication, which resulted in minimal cracks in the Ti-based alloy.

Hardness Results

Figure 5 displays the microhardness of the Ti-Fe-Si-Nb-Cr alloy produced at different laser processing parameters. Figure 5a–c and d shows the profile and average microhardness of the alloys with varying alloy depth, respectively. According to Fig. 5a–c, the microhardness of the alloys decreases along the distance of measurements towards the substrates for all processing parameters. As discussed under Section “Phase Formation and Microstructural Evolution”, the decrease in the cooling rate from the top to the bottom of the alloy induces grain growth in the same direction. The laser power of 750 W yielded an alloy with the highest microhardness compared to those obtained at 950 W and 1150 W. The increase in laser scanning speed from 0.4 m/min to 1.2 m/min also

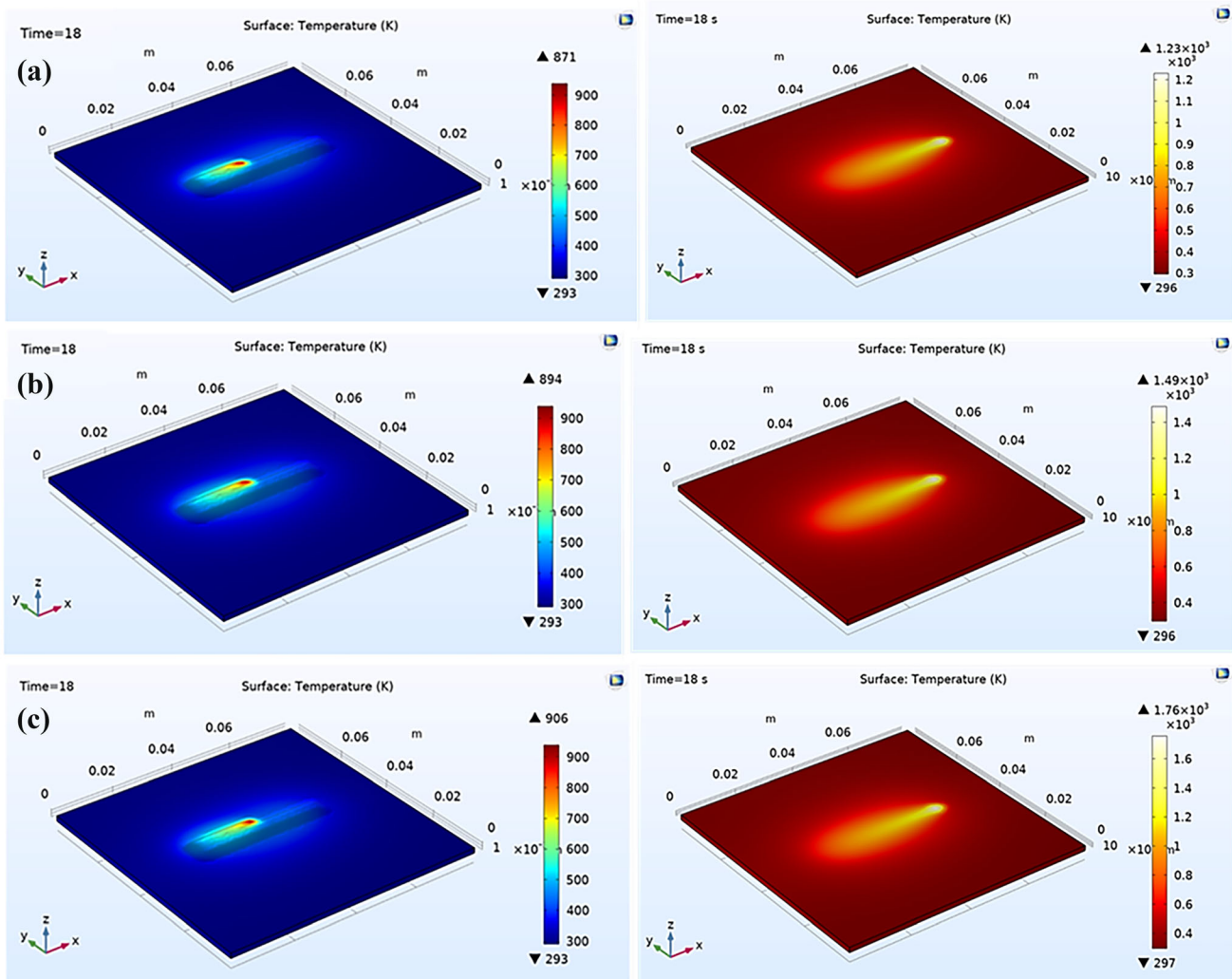


Fig. 4. Thermal behavior of the Ti-Fe-Si-Cr-Nb alloy at 1.2 the m/min for different laser powers of: (a) 750 W, (b) 950 W, and (c) 1150 W.

showed a significant positive shift in hardness. The highest microhardness value of 634 HV was obtained at a laser power of 750 W and scanning speed of 1.2 m/min. Changing the scanning speed from 0.4 m/min to 1.2 m/min increases the microhardness from 587 HV to 634 HV and 547 HV to 607 HV for alloys produced at 750 W and 1150 W laser powers, respectively. However, this behavior was not observed for samples fabricated at 950-W laser power. These results are supported by the optical microscopy micrographs shown in Fig. 2, where refinement of grains occurred as a result of a reduction in energy density. According to the Hall-Petch equation, the strength of a material is indirectly proportional to the size of the grains. Lower energy densities may also increase the amount of unmelted particles. The presence of these particles in the melt pool may promote nucleation of new grains and lead to the formation of microstructures with refined grains. On the other hand, the deviation in behavior for samples fabricated at a

laser power of 950 W may be due to the negligible difference in energy density.

Tribological Behavior

Figure 6 shows the friction coefficient of Ti-Si-Fe-Cr-Nb alloys obtained at different laser processing parameters. From the figure, it can be seen that the friction coefficients of the samples fabricated at all processing parameters are lower than 0.35. It can also be seen that alloys fabricated at low scanning speeds are characterized by low friction coefficients for all laser powers. The alloy produced at 750 W and 0.4 m/min maintained a friction coefficient of less than 0.18 for the total duration of the test. The results obtained can be ascribed to the high energy density associated with these conditions, which promote the formation of a ductile Ti_5Si_3 precipitate which may provide a lubricating effect during wear. This tends to reduce friction between the stainless steel ball of the tribometer and the material being subjected to wear testing, resulting in wear loss

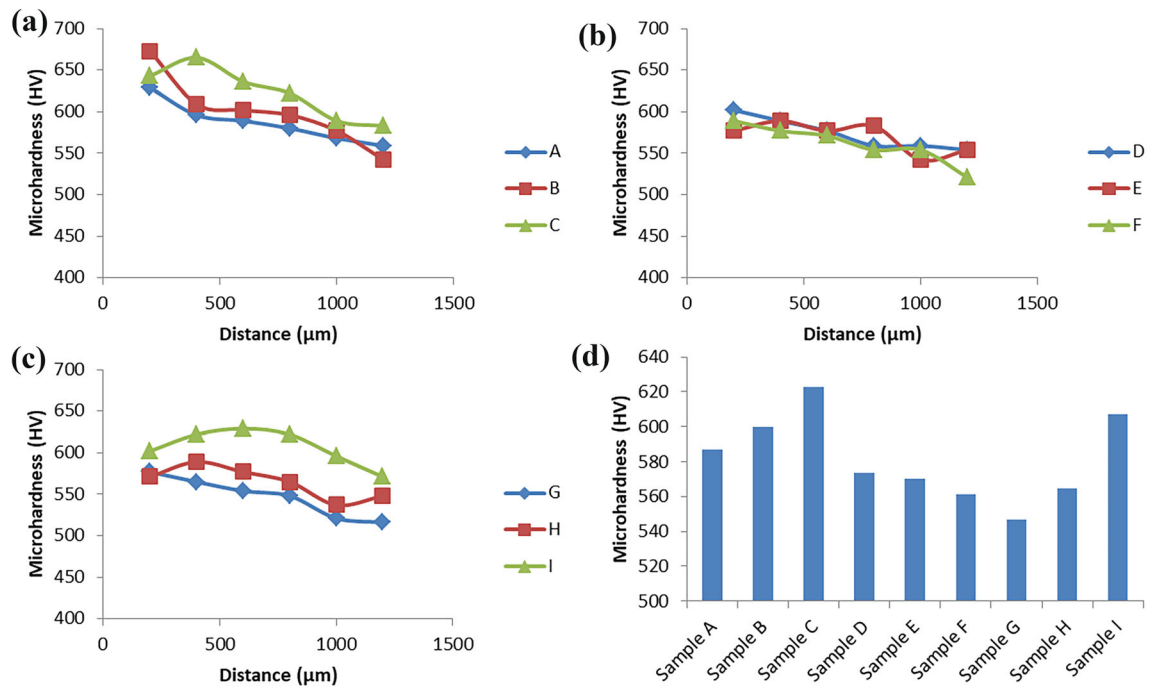


Fig. 5. Hardness values for alloys fabricated at scanning speeds of 0.4, 0.8, and 1.2 m/min and laser powers of: (a) 750 W; (b) 950 W; and (c) 1150 W; (d) average microhardness.

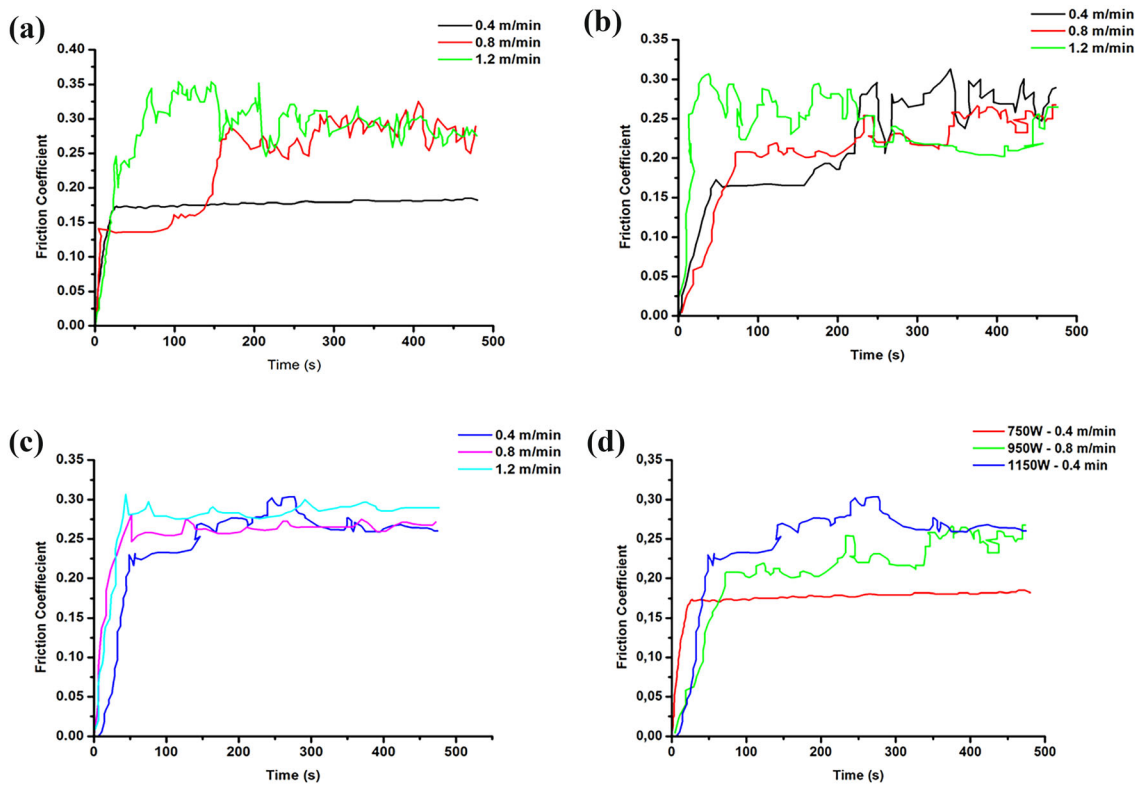


Fig. 6. Variation in friction coefficients of Ti-Si-Fe-Cr-Nb alloy due to time for samples fabricated at (a) 750 W, (b) 950 W, (c) 1150 W, and (d) all laser powers with a scanning speed of 0.4 m/min.

reduction. High fluctuation in the coefficient of friction was also observed over time. The samples fabricated at 950 W and 1150 W with the same

scanning speed maintained lower values for the period of time less than 200 s and, beyond this, an increase in the coefficient of friction was noticed.

The wear loss of the laser deposited samples is presented in Fig. 7, and is the amount of the material removed by the steel ball test piece from the surface of the samples. The results obtained are in agreement with the friction behavior exhibited by the samples as shown in Fig. 6. Samples fabricated at low laser scanning speeds showed minimal wear loss of a maximum of 0.1 mg, except for those produced at a laser power of 950 W. All the samples which showed high wear resistance had the least microhardness properties. This is in conflict with the results that have been obtained by many authors where high hardness corresponded to improved wear resistance. High microhardness was reported to improve resistance to plastic deformation and lead to low material loss. However, the deviation of the results obtained in this work might be due to the high brittleness possessed by the samples produced at high scanning speeds. As can be seen in Fig. 2, the samples were characterized by several defects, such as cracks and pores. The combined effect of brittleness and the presence of cracks initiates fragmentation when subjected to high loads and causes severe wear damage.⁶

The SEM images in Fig. 8 show the worn morphology surfaces of the samples fabricated at all laser processing parameters. It is evident from the images that the wear damage on the surface of the alloy samples was caused by abrasive and adhesive wear, showing that the Ti-Fe-Si-Cr-Nb alloy exhibited high wear resistance due to the large amount of α -phase present. Thus, enhanced wear resistance was achieved for the alloys due to good toughness. However, microplothing and grooving are evident in samples that possessed higher hardness values owing to the β - and Ti_5Si_3 -phases present. The

furrows and groves are deeper and wider compared to those with lower hardness.

CONCLUSION

A Ti-Fe-Si-Cr-Nb alloy was successfully fabricated by means of LMD technique on Ti6Al4V substrates. The effect of laser processing parameters on the microstructural evolution, phase formation, microhardness, and wear behavior was investigated and the following conclusions were drawn:

- The fabricated samples showed good metallurgical bonding with the substrates, but cracks or crack initiation was visible in optical micrographs and SEM images of the microstructure on the surface of samples produced at laser power of 750 W. However, with low scanning speeds and high laser powers of 950 W and 1150 W, the samples build-up (or thickness) were higher, with negligible surface cracks observed. Thus, at low laser scanning speeds, heat input is increased resulting in a simultaneous increase in energy densities.
- The fabricated alloy exhibited α -Ti as a major phase and the β -phase, along with Ti_5Si_3 intermetallic phases formed with the α -phase having the highest volume fraction with a bcc. The β - and Ti_5Si_3 -phases contribute immensely to strengthening mechanisms of the alloy through dispersion strengthening caused by reinforcements, solid-solution strengthening, and elastic mismatching of the reinforcing phases and the α -Ti matrix. However, the dispersion strengthening provided the most significant strengthening effect.
- The computation model results demonstrated

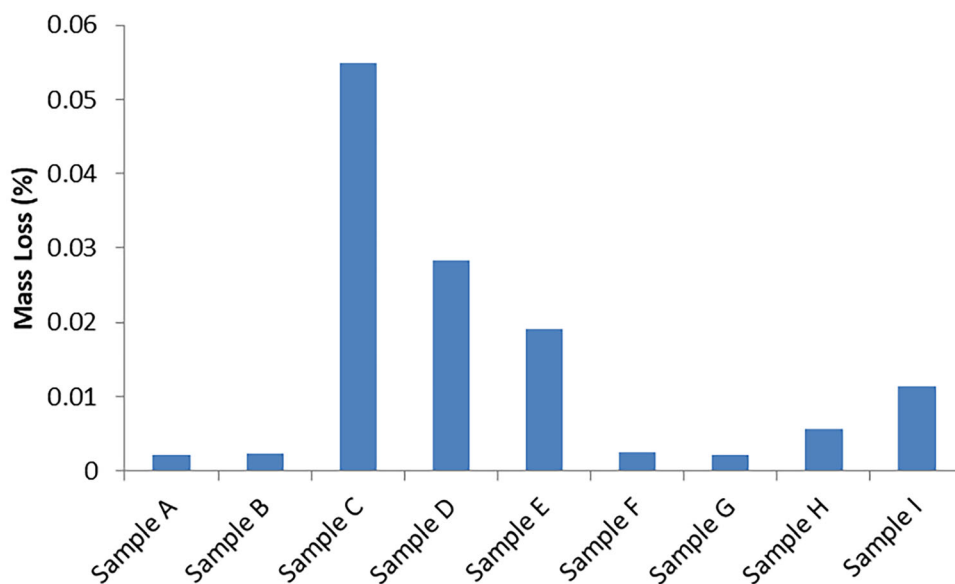


Fig. 7. Wear loss for samples fabricated at all laser processing parameters.

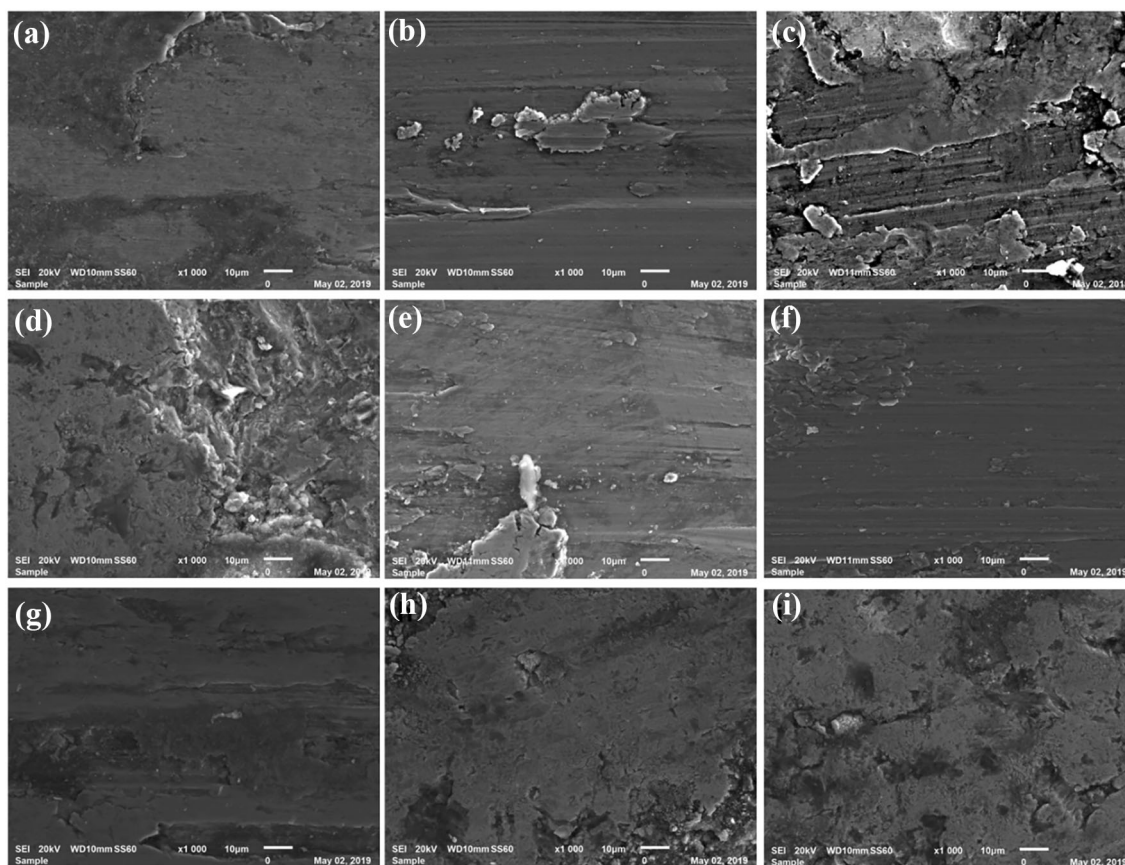


Fig. 8. Wear scars for samples fabricated at: 750 W (a) 0.4, (b) 0.8, and (c) 1.2 m/min; 950 W (d) 0.4, (e) 0.8, and (f) 1.2 m/min; and 1150 W (g) 0.4, (h) 0.8, and (i) 1.2 m/min.

that a high laser power significantly influences the reduction of cracks and refining the grains of the microstructure owing to the increased surface temperature.

- The average microhardness of Ti-Fe-Si-Cr-Nb alloys produced by 750-W laser power were higher when compared to the average microhardness values obtained for samples fabricated at 950 W and 1150 W with scan speed of 1.2 m/min.
- The SEM images of the worn morphology showed that the Ti-Fe-Si-Cr-Nb alloy exhibited high wear resistance. The wear mechanism of the alloy is a mixture of abrasive and adhesive wear with samples having high hardness owing to the β - and Ti_5Si_3 -phases present. However, improvement in wear resistance occurs due to the large quantity of α -phase present.

ACKNOWLEDGEMENTS

The authors would like to show their appreciation to the following organizations: Council of Scientific and Industrial Research (CSIR), National Research Foundation (NRF) with Surface Engineering Research Laboratory (SERL), Tshwane University of

Technology, Department of Chemical, Metallurgical and Materials Engineering, Pretoria, South Africa.

FUNDING

Open access funding provided by Tshwane University of Technology.

CONFLICT OF INTEREST

On behalf of all authors, the corresponding author states that there is no conflict of interest

OPEN ACCESS

This article is licensed under a Creative Commons Attribution 4.0 International License, which permits use, sharing, adaptation, distribution and reproduction in any medium or format, as long as you give appropriate credit to the original author(s) and the source, provide a link to the Creative Commons licence, and indicate if changes were made. The images or other third party material in this article are included in the article's Creative Commons licence, unless indicated otherwise in a credit line to the material. If material is not included in the article's Creative Commons licence and your intended use is not permitted by statutory

regulation or exceeds the permitted use, you will need to obtain permission directly from the copyright holder. To view a copy of this licence, visit <http://creativecommons.org/licenses/by/4.0/>.

REFERENCES

1. Y. Feng, K. Feng, C. Yao, Z. Li, J. Sun, and J. Mat, *Mater. Des.* 157, 258 (2018).
2. K.A. Nazari, R.R. Rashid, S. Palanisamy, K. Xia, and M. Dargusch, *Mater. Lett.* 229, 301 (2018).
3. S. Zhou, Y. Xu, B. Liao, Y. Sun, and X. Dai, *J. Alloys Compd.* 768, 697 (2018).
4. Z. Zhao, J. Chen, S. Guo, H. Tan, X. Lin, and W. Huang, *J. Mater. Sci. Technol.* 33, 675 (2017).
5. L. Jian and H. Wang, *Surf. Coat. Technol.* 192, 305 (2005).
6. R.L. Sun, D.Z. Yang, L.X. Guo, and S.L. Dong, *Surf. Coat. Technol.* 132, 251 (2000).
7. P. Li, H. Zhang, T. Tong, and Z. He, *J. Alloys Compd.* 786, 986 (2019).
8. C.R.M. Afonso, A.I. Vidilli, J.E. Spinelli, R. Riva, V. Amigo, and C.S. Kiminami, *Surf. Coat. Technol.* 328, 161 (2017).
9. C.D. Rabadia, Y.J. Liu, L. Wang, H. Sun, and L.C. Zhang, *Mater. Des.* 154, 228 (2018).
10. Z.G. Liu, X. Wang, X.P. Wang, C.J. Zhang, L.H. Chai, and Y.Y. Chen, *J. Alloys Compd.* 504S, S480 (2010).
11. G.-H. Zhao, S.V. Ketov, H. Mao, A. Borgenstam, and D.V. Louzguine-Luzgin, *Scr. Mater.* 135, 59 (2017).
12. C.D. Rabadia, Y.J. Liu, G.H. Cao, Y.H. Li, C.W. Zhang, T.B. Sercombe, H. Sun, and L.C. Zhang, *Mater. Sci. Eng. A* 732, 368 (2018).
13. M. Fischer, P. Laheurte, P. Acquier, D. Joguelet, L. Peltier, T. Petithory, K. Anselme, and P. Mille, *Mater. Sci. Eng. C* 75, 341 (2017).
14. G.H. Zhao, S.V. Ketov, J. Jiang, H. Mao, A. Borgenstam, and D.V. Luizguine-Luzgin, *Mater. Sci. Eng. A* 705, 348 (2017).
15. C. Wang and C. Dong, *Mater. Today Commun.* 3, 43 (2015).
16. B. Carcel, A. Serrano, J. Zambrano, V. Amigo, and A.C. Carcel, *Phys. Procedia* 56, 284 (2014).
17. H.M. Wang and Y.F. Liu, *Mater. Sci. Eng. A* 338, 126 (2002).
18. S.A. Raji, A.P.I. Popoola, S.L. Pityana, and M. Tlotleng, *J. Mater. Eng. Perform.* 30, 3321 (2021).
19. S.A. Raji, A.P.I. Popoola, S.L. Pityana, O.M. Popoola, N.K. Raji, and M. Tlotleng, In-situ LENS fabricated Ti-Al-Si alloy phase transformation and microstructural evolution after isothermal annealing heat treatments, in *Paper presented at TMS 2022 151st Annual Meeting & Exhibition Supplemental Proceedings* (2022), p. 313.
20. J. Dai, F. Zhang, A. Wang, H. Yu, and C. Chen, *Surf. Coat. Technol.* 309, 805 (2017).
21. I. Mathoho, E. Akinlabi, N. Arthur, and M. Tlotleng, *CIRP J. Manuf. Sci. Technol.* 31, 450 (2020).
22. C. Hong, D. Gu, D. Dai, M. Alkhatay, W. Urban, P. Yuan, S. Cao, A. Gasser, A. Weisheit, I. Kelbassa, and M. Zhong, *Mater. Sci. Eng. A* 635, 118 (2015).
23. X. Zhang, C. Li, M. Zheng, Z. Ye, and X. Yang, *J. Gu. Addit. Manuf.* 32, 101087 (2020).
24. L.E. Murr, S.M. Gaytan, A. Ceylan, E. Martinez, J.L. Martinez, D.H. Hernandez, B.I. Machado, D.A. Ramirez, F. Medina, S. Collins, and R.B. Wicker, *Acta Mater.* 58, 1187 (2010).
25. M. Li, X. Wu, Y. Yang, Q. Wei, C. Yan, C. Cai, J. Liu, W. Li, and Y. Shi, *Mater. Charact.* 143, 197 (2018).
26. M. Seifi, A.A. Salem, D.P. Satko, U. Ackelid, S.L. Semiatin, and J.J. Lewandowski, *J. Alloys Compd.* 729, 1118 (2017).
27. A. Seidel, S. Saha, T. Maiwald, J. Moritz, S. Polenz, A. Marquardt, J. Kaspar, T. Finaske, E. Lopez, F. Brueckner, and C. Leyens, *JOM* 71, 1513 (2019).
28. M. Simonelli, D.G. McCartney, P. Barriobero-Vila, N.T. Aboulkhair, Y.Y. Tse, A. Clare, and R. Hague, *Metall. Mater. Trans. A* 51, 2444 (2020).
29. P. Gao and Z. Wang, *Mater. Sci. Eng. A* 780, 139183 (2020).
30. M. Tlotleng, *J. Mater. Eng. Perform.* 28, 701 (2019).

Publisher's Note Springer Nature remains neutral with regard to jurisdictional claims in published maps and institutional affiliations.